Noncollinear ferrielectricity and hydrogen-induced ferromagnetic polar half-metallicity in MnO₃Cl

Xinyu Yang ●, Jun Chen ●, Shan-Shan Wang ●,* and Shuai Dong ●†

Key Laboratory of Quantum Materials and Devices of Ministry of Education, School of Physics,
Southeast University, Nanjing 211189, China

Collinear dipole orders such as ferroelectricity and antiferroelectricity have developed rapidly in recent decades, while the noncollinear dipole orders are rarely touched in solids. Noncollinear dipole orders can provide a route to realize ferrielectricity. Based on first-principles calculations, an inorganic molecular crystal MnO₃Cl has been demonstrated to own intrinsic noncollinear ferrielectricity, which originates from the stereo orientations of polar molecules. The large negative piezoelectricity effect ($d_{33} \sim -27$ pC/N) is also predicted. A strong light absorption and moderate optical anisotropy are found for this molecular crystal in the ultraviolet-light window. Additionally, by electron doping via hydrogen intercalation, a ferromagnetic polar half-metal can be obtained. This study provides a material platform to explore the intriguing physics of noncollinear ferrielectricity and potential applications in devices.

I. INTRODUCTION

Ferroic materials, possessing switchable vectors such as polarization and magnetization, are a favorite topic in the condensed matter community and for potential applications in memory devices [1–6]. In the framework of Landau-Ginzburg theory, the magnetic and electrical dipole orders have a one-to-one correspondence. In magnets, both collinear and noncollinear magnetic orders have been extensively investigated [7–9]. Much progress has been reported towards the noncollinear magnetism, which can give rise to various physical properties, including the anomalous Hall effect, skyrmions, and magneto-optical Kerr effects [10–12]. However, noncollinear polarizations remain in the early stage. In addition, the noncollinear dipole texture contains the ferroelectric (FE) and antiferroelectric (AFE) modes, which can lead to ferrielectricity. Until now, only a few works have focused on it. It is found that the noncollinear dipole order has been realized in perovskite deviants in experiments [13,14]. Theoretical study predicts that strained BiFeO₃ can exhibit noncollinear ferrielectric polarization [15–17]. Very recently, a two-dimensional dioxydihalide family was also predicted to display intrinsic noncollinear ferrielectricity and thus generate topological domains and negative piezoelectricity, but this is yet to be verified by experiments [18]. The lack of material platforms makes it hard to uncover the underlying physical mechanism of noncollinear electrical dipole orders. In this scenario, it is extremely necessary to broaden the types of noncollinear polar materials to thoroughly study the unexplored properties.

On the other hand, molecular ferroelectricity has undergone a rapid development and attracted extensive attention due to its structural flexibility, biocompatibility, and light weight [19–23]. Much effort has been devoted to the organic molecular ferroelectricity, but the noncollinearity mostly comes from the stereochemical structure of bulky organic groups. Then the switching of the canting dipole would be relatively slow and the switching path would be complex. Compared with the organic molecules, the pure inorganic molecules have a very small molecular unit, which may provide the feasibility for fast switching comparable to that widely used in inorganic ferroelectric perovskites. Such noncollinear dipoles in pure inorganic molecules are not common.

Recently, an inorganic molecular bulk with high valence manganese (Mn⁷⁺) atoms, MnO₃Cl, was successfully synthesized in experiment [24]. The MnO₃Cl is made up of tetrahedral polar molecular units with weak intermolecular interactions, which may provide an ideal material platform to explore noncollinear dipole orders.

In this work, based on first-principles calculations and Monte Carlo (MC) simulations, we demonstrated that MnO₃Cl displays a different type of noncollinear ferrielectric order. A special switchable path of electric polarization through the molecular rotation-flip model has been constructed. In addition, the intriguing negative piezoelectric effect and optical properties are also revealed in this molecular crystal. Upon intercalating hydrogen atoms to their interstitial positions, there is a distinct transition from nonmagnetic ferrielectricity to ferromagnetic polar half-metallicity, where 100% spin polarization and polarity coexist in the single crystal Mn(OH)₃Cl.

II. COMPUTATIONAL METHODS

First-principles calculations based on density functional theory (DFT) are performed with the projector augmented-wave (PAW) pseudopotentials as implemented in the Vienna *ab initio* Simulation Package (VASP) [25]. The exchange-correlation functional is treated using Perdew-

———————
*Contact author: wangss@seu.edu.cn
†Contact author: sdong@seu.edu.cn

TABLE I. The structure parameters of MnO_3Cl. The tested exchange-correlation functionals are GGA-PBE and Perdew-Burke-Ernzerhof-revised (PBEsol) of GGA. The experimental results (Expt.) are listed for comparison. a, b, and c are in units of Å. Notably, the GGA-PBE correction makes the lattice constants closer to the experimental values.

	a	b	c
Expt. [24]	7.155	10.084	5.009
GGA-PBE	6.985	10.166	5.000
GGA-PBEsol	6.626	9.909	4.782

Burke-Ernzerhof (PBE) parametrization of the generalized gradient approximation (GGA) [26]. More tests with different exchange-correlation functionals can be found in Table I. The energy cutoff is fixed to 500 eV. The Γ-centered $4 \times 3 \times 6$ Monkhorst-Pack k mesh is adopted. The van der Waals (vdW) correction DFT-D3 method is applied [27]. The convergence criterion for the energy is 10^{-6} eV for self-consistent iteration, and the Hellman-Feynman force is set to 0.01 eV/Å during the structural optimization. Ferrielectric polarization is calculated using the standard Berry phase method [28].

The EXCITING package is adopted to calculate the nonlinear optical susceptibility tensors for the second-harmonic generation (SHG) of MnO_3Cl [29]. During the SHG calculation, the tolerance factor is set as 1×10^{-3} to avoid singularities.

The optical parameters are performed using the frequency-dependent dielectric functions expressed as $\epsilon(\omega) = \epsilon_1(\omega) + i\epsilon_2(\omega)$. And the optical absorption coefficient $\alpha(\omega)$ has a relationship with the real part of the dielectric function $\epsilon_1(\omega)$ and the imaginary component $\epsilon_2(\omega)$:

$$\alpha(\omega) = \frac{2\sqrt{2}\pi E}{hc}\left[\sqrt{\epsilon_1^2(\omega) + \epsilon_2^2(\omega)} - \epsilon_1(\omega)\right]^{\frac{1}{2}}, \quad (1)$$

where E is the incident photon energy, h is the Planck constant, and c is the speed of light in vacuum. $\epsilon_1(\omega)$ and $\epsilon_2(\omega)$ can also be used to calculate the refractive index $n(\omega)$ and the extinction coefficient $k(\omega)$ using the following equations [30]:

$$n(\omega) = \frac{1}{\sqrt{2}}\left[\sqrt{\epsilon_1^2(\omega) + \epsilon_2^2(\omega)} + \epsilon_1(\omega)\right]^{\frac{1}{2}}, \quad (2)$$

$$k(\omega) = \frac{1}{\sqrt{2}}\left[\sqrt{\epsilon_1^2(\omega) + \epsilon_2^2(\omega)} - \epsilon_1(\omega)\right]^{\frac{1}{2}}. \quad (3)$$

Considering that the PBE function usually underestimates the band gap of the semiconductor, we carry out a PBE-level optical properties calculation with a corrected parameter $\Delta E_{g,\text{HSE}}$, i.e., the energy difference between the PBE band gap and Heyd-Scuseria-Ernzerhof hybrid functional band gap [31].

For the $Mn(OH)_3Cl$, the Hubbard U is applied using the Dudarev parametrization [32]. As previously reported, a correction of $U_{\text{eff}} = 3$ eV is imposed on Mn's $3d$ orbitals [33]. In addition, the *ab initio* molecular dynamics (AIMD) simulation in the NVT ensemble lasts for 6 ps with a time step of 2 fs. The Nose-Hoover method is used for temperature control. [34]. Moreover, the MC simulations based on the Heisenberg model are applied to estimate the magnetic transition temperatures. An $18 \times 18 \times 18$ lattice with periodic boundary condition is
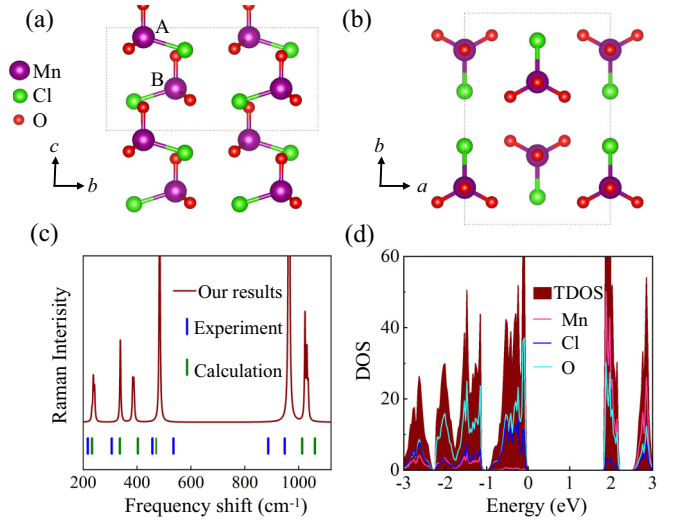

FIG. 1. (a),(b) The side and top views of the MnO_3Cl crystal. The primitive cell is indicated by the black dotted rectangles. (c) The DFT-calculated Raman spectra of an MnO_3Cl crystal. The characteristic peak points of previously reported values (experiment and calculation) are shown as bars for comparison. (d) The projected density of states (pDOS) structure of an MnO_3Cl crystal.

adopted in the MC simulations. The initial 5×10^4 MC steps (MCSs) are performed for thermal equilibrium, then another 5×10^4 MCSs are reserved as the statistical average.

III. RESULTS AND DISCUSSION

A. Noncollinear ferrielectricity

The MnO_3Cl single crystal consists of unique zero-dimensional (0D) structures, which extend into three-dimensional (3D) molecular frameworks through the weak vdW interactions. Each MnO_3Cl owns a dipole, pointing along the Mn-Cl bonding direction (mainly along the b axis). The dipole-dipole interactions prefer (1) the antiparallel alignment between side-by-side neighbors (A and B) along the c axis, and (2) the parallel alignment between head-to-tail neighbors (A and A′) along the b axis, as displayed in Fig. S1 of the Supplemental Material (SM) [35].

However, this collinear dipole order is not the most stable one. As shown in Fig. S1 in the SM [35], the antiphase canting of the upper and lower molecules (A and B) can reduce the energy for 0.17 eV/f.u. (at 17.4°). Such energy reduction can be intuitively attributed to the Coulomb repulsion. After canting, the nearest O1-O9 distance between A and B is enlarged, while the nearest Cl2-O9 distance between A and B is shortened. By inputting the concrete values, a rough estimation leads to a positive energy gain from such molecular canting. The stable structure within a unit cell is depicted in Figs. 1(a) and 1(b). It has a polar space group of $Cmc2_1$ with mirror and twofold rotation symmetries. According to our calculation, the optimized lattice constant is in agreement with the experiment (see Table I) [24]. Furthermore, the DFT-calculated Raman spectra of the MnO_3Cl crystal is also consistent with previously reported values, as shown in Fig. 1(c). Figure 1(d) displays its projected density of states
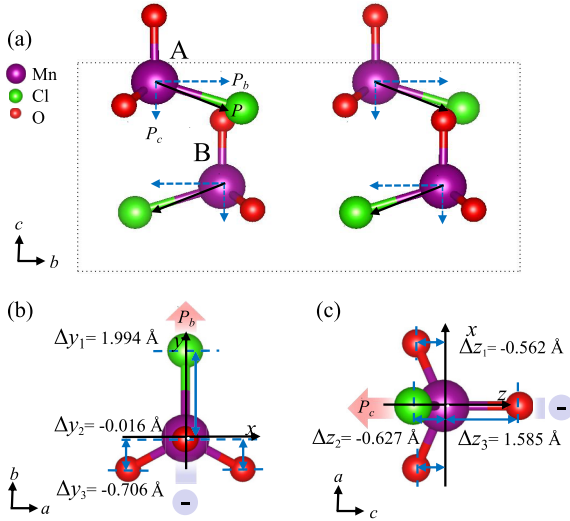
FIG. 2. (a) Schematic of ferrielectric polarization in an MnO_3Cl crystal. The b components of molecules A and B are compensated, while the c components are parallel. Taking the molecule A for an example: (b) View from the c axis. The b-axis projected distances between O^{2-}/Cl^- and Mn^{7+} are denoted as Δy_1, Δy_2, Δy_3. Then, $d_b = -\Delta y_1 - 2\Delta y_2 - 4\Delta y_3 = 0.862 \, |e|Å$, implying a net dipole along the b direction. (c) View from the b axis. The c-axis projected distances between O^{2-}/Cl^- and Mn^{7+} are denoted as Δz_1, Δz_2, Δz_3. Then, $d_c = -4\Delta z_1 - \Delta z_2 - 2\Delta z_3 = -0.295 \, |e|Å$, implying a net dipole along the $-c$ direction.

FIG. 3. (a) The energy barrier and polarization of a possible ferrielectric switching path as a function of the canting angle θ of the Mn-Cl bond from the b axis for a MnO_3Cl crystal. (b) A comparison of the calculated SHG angular plots of MnO_3Cl and KH_2PO_4 crystals on the bc plane with 1064 nm light. (c) Optical absorption spectra. Solid lines of different color represent the calculated results for MnO_3Cl (red and blue lines for polarization of light in the ac plane and green line for polarization of light out-of-plane along the b axis). Visible region: 1.65–3.26 eV [31]. (d) Anisotropic optical properties of the MnO_3Cl crystal. Birefringence: $\Delta n_{ij} = n_j - n_i$; dichroism: $\Delta k_{ij} = k_j - k_i$. Here, i and j are any two orthogonal crystal axes: a, b, and c.

structure, indicating a semiconductor state with band gap of $\sim$1.83 eV. It is noted that electronic localization shows peak effects, and the peak effect at the Fermi level is mainly contributed by the O-p orbital, suggesting its potential for efficient light absorption (to be discussed later).

Each MnO_3Cl molecule contributes a dipole (d), as shown in Fig. 2, which can be estimated as

$$\mathbf{d}_{ij} = \sum_j \Delta \mathbf{r}_{ij} q_j, \qquad (4)$$

where q_j is the charge of O^{2-}/Cl^- ions, and $\Delta \mathbf{r}_{ij}$ represents the offset vector of O^{2-}/Cl^- relative to Mn^{7+}. Then the value of $\mathbf{d}$ is estimated as $(0, 0.862, -0.295) \, |e|Å$ for molecule A, while it is $(0, -0.862, -0.295) \, |e|Å$ for molecule B.

Among the whole bulk structure, it displays a surprising noncollinear ferrielectric texture with the partial compensation of dipoles, namely, the b components of dipoles are compensated, but the c components of dipoles lead to a net switchable polarization. Therefore, it can exhibit both ferroelectric (P_c: ferroelectric order parameter) and antiferroelectric (P_b: antiferroelectric order parameter) behaviors. These two components are coupled via the geometric relationship $P_b^2 + P_c^2 = P^2$, where P is almost a constant of the MnO_3Cl molecule.

Besides the intuitive estimation based on the point charge mode, we also calculated the rigorous polarization using the Berry phase method as implemented in VASP, which leads to 2.1 $\mu C/cm^2$ along the opposite direction of the c axis in the MnO_3Cl crystal. Thus the direction of the dipole is consistent between the point charge model and Berry phase method. The
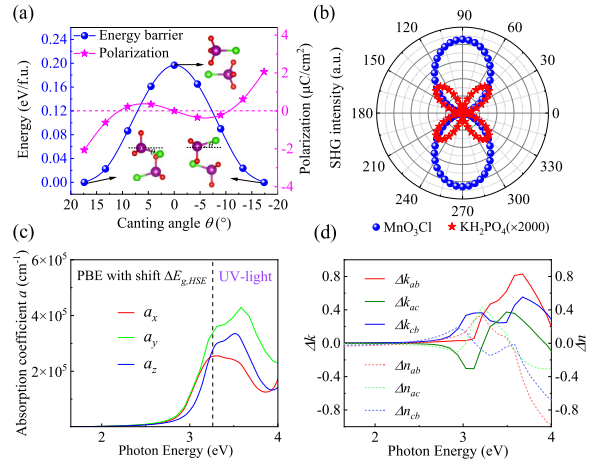
value of polarization is comparable with that of $CuInP_2S_6$ (2.55 $\mu C/cm^2$) [36].

The switching of polarization is another important property for ferroic materials. As shown in Fig. 3(a), the ferrielectric switching process is also estimated using the climbing image nudged elastic band (CINEB) method [37]. Assuming an electric field is applied along the polarization direction, polar molecules may rotate around the a axis, leading to the net polarization flipping. Apart from alterations in bond angles, bond lengths also undergo corresponding changes (see Fig. S2 in the SM [35]). The energy barrier of transformation proceeds through an antiferroelectric configuration (space group $P2_1/m$). And the switching energy barrier between the ferrielectric state and antiferroelectric state is ~ 0.2 eV/f.u., suggesting the ferrielectric stability and switchability.

In practice, the optical second-harmonic generation (SHG) is a sensitive and nondestructive tool to characterize non-centrosymmetric materials [38,39], in particular vital for ferrielectric materials. The lack of spatially inversion symmetry in MnO_3Cl crystals allows the intrinsic SHG signal. Here, the nonlinear optical susceptibility tensors (d_{ij}) can be expressed as a 3 × 6 matrix [40]:

$$d = \begin{bmatrix} 0 & 0 & 0 & 0 & d_{15} & 0 \\ 0 & 0 & 0 & d_{24} & 0 & 0 \\ d_{31} & d_{32} & d_{33} & 0 & 0 & 0 \end{bmatrix}. \qquad (5)$$

Then, the second-harmonic polarization $P^{2\omega}$ can be expressed as [41]

$$
\begin{bmatrix} P_a^{2\omega} \\ P_b^{2\omega} \\ P_c^{2\omega} \end{bmatrix} = 2 \times \begin{bmatrix} 0 & 0 & 0 & 0 & d_{15} & 0 \\ 0 & 0 & 0 & d_{24} & 0 & 0 \\ d_{31} & d_{32} & d_{33} & 0 & 0 & 0 \end{bmatrix} \begin{bmatrix} E_a^2 \\ E_b^2 \\ E_c^2 \\ 2E_bE_c \\ 2E_aE_c \\ 2E_aE_b \end{bmatrix}
$$

$$
= 2 \times \begin{bmatrix} 2d_{15}E_aE_c \\ 2d_{24}E_bE_c \\ d_{31}E_a^2 + d_{32}E_b^2 + d_{33}E_c^2 \end{bmatrix}, \tag{6}
$$

where ω is the wave of frequency. Here, $a/b/c$ are perpendicular crystalline axes. The SHG intensity I can be estimated as [40]

$$
I \propto (P^{2\omega})^2 = \left(P_a^{2\omega}\right)^2 + \left(P_b^{2\omega}\right)^2 + \left(P_c^{2\omega}\right)^2. \tag{7}
$$

For MnO_3Cl under perpendicular incident light on the bc plane, the polarization vector can be expressed as $\boldsymbol{E} = (E_a, E_b, E_c) = E(0, \cos\phi, \sin\phi)$. The SHG intensity can be expressed as $I \propto (2d_{24}\sin 2\phi)^2 + (2d_{32}\cos^2\phi + 2d_{33}\sin^2\phi)^2$, where ϕ is the angle between the crystalline b axis and the electric field direction of incident light. Similarly, the SHG intensity of KH_2PO_4 on its bc plane can be written as $I \propto (2d_{14}\sin 2\phi)^2$.

The calculated SHG tensors d_{ij} of MnO_3Cl bulk at a wavelength of 1064 nm (which is frequently used in SHG experiments) are shown in Fig. S3 of the SM [35], in comparison with a frequently used reference KH_2PO_4 [42]. Furthermore, the SHG angular plot of MnO_3Cl is calculated using these tensors; as shown in Fig. 3(b), it presents a bipolar behavior and the strongest signal appears when the angle ϕ reaches $90°$ (the polarization direction of the incident light is along the c axis), which is much stronger than that of KH_2PO_4.

B. Negative piezoelectricity and optical properties

Negative piezoelectricity refers to the phenomenon in which the polarization increases when the lattice is shrinking along the polarization direction. This exotic physical property is important in the study of ferroelectric/ferrielectric materials, but is rarely observed in experiments [43,44]. To investigate the piezoelectricity in this noncollinear ferrielectricity, piezoelectric stress coefficients e_{ik} are calculated using the density functional perturbation theory (DFPT) method [45]. There are five independent nonzero piezoelectric stress coefficients e_{ik} in the piezoelectric tensor matrix for point group $mm2$ [46]:

$$
e = \begin{bmatrix} 0 & 0 & 0 & 0 & 0.12 & 0 \\ 0 & 0 & 0 & 0.06 & 0 & 0 \\ 0.09 & 0.02 & -0.28 & 0 & 0 & 0 \end{bmatrix}. \tag{8}
$$

The calculated e_{33} is -0.28 C/m^2. There is a stronger dipole moment within a smaller volume due to the joint contribution of the noncollinear dipole orders and the intermolecular effects between the 0D polar molecules. In

TABLE II. Calculated energies (in units of meV/f.u.) of different stacking models (α state vs β state) with four possible magnetic orders in the $Mn(OH)_3Cl$ crystal. The β state with FM order is taken as the reference, which has the lowest energy. AFM: antiferromagnetic. FM: ferromagnetic.

	AFM 1	AFM 2	AFM 3	FM
α state	207.02	183.55	204.39	178.29
β state	25.29	2.04	24.85	0

addition, the elastic stiffness tensors (C_{kj}) are calculated by the energy-strain method using VASPKIT [47], which can be found in the SM [35]. Then the piezoelectric strain coefficients d_{ij} can be determined as follows:

$$
d_{ij} = \sum_{k=1}^{6} e_{ik}C_{kj}^{-1}. \tag{9}
$$

The longitudinal strain coefficient d_{33} is -27.37 pC/N, which is 19 times that of ZrI_2 (-1.445 pC/N) [48], indicating a large negative piezoelectricity.

Another noteworthy characteristic is the optical absorption of MnO_3Cl, as previously mentioned. The orthorhombic crystal MnO_3Cl has three principal dielectric constants: $\varepsilon_{xx} \neq \varepsilon_{yy} \neq \varepsilon_{xx}$. We label them as ε_a, ε_b, and ε_c, respectively, as calculated in Fig. S4 of the SM [35]. Figure 3(c) shows the calculated optical absorption coefficient α as a function of photon energy in MnO_3Cl. The first peak of the optical absorption spectrum can be seen in the energy windows of ultraviolet light (UV light) and the absorption coefficient of light polarization along the b axis reaches a large magnitude ($\sim 10^5$ cm^{-1}), implying its strong UV-light absorption. Additionally, birefringence and dichroism can be utilized to assess optical anisotropy of the optical properties, quantifying the difference between any two components of n and k along the principal crystal axes. Figure 3(d) shows that anisotropy exists along the b direction, as reflected by the large positive values (Δk_{ab}, Δk_{cb}) in the energy range of 3.26–4.0 eV and high values of Δn_{ab} and Δn_{cb}.

C. Ferromagnetic polar half-metallicity

In general, the screening effect of free carriers on dipole-dipole interaction makes it difficult for the coexistence of metallic properties and polarization. Moreover, it is even more challenging to form ferromagnetic polar half-metals with appropriate electronic structures [49,50].

The MnO_3Cl crystal with Mn's $3d^0$ configuration behaves nonmagnetically. However, the variable valence of Mn provides the feasibility to induce its magnetism via electron doping. As mentioned before, MnO_3Cl crystal is spatially loose due to the vdW interactions, which possesses adequate interstitial positions for intercalating hydrogen atoms [51–53]. Considering all possible H intercalation positions of MnO_3Cl and different stacking modes (α state vs β state), we optimized all of the possible structures. $Mn(OH)_3Cl$ undergoes a structural reconstruction during the relaxation. H-intercalation causes two molecules with tetrahedral configurations to combine into a conventional octahedron, as
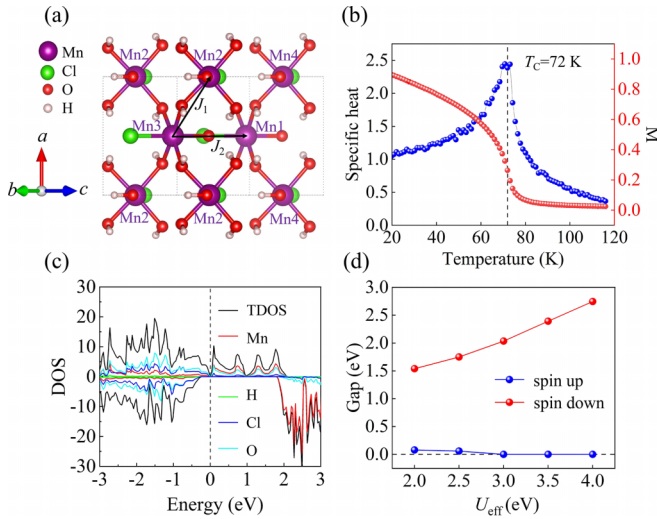
FIG. 4. (a) Exchange J's are indicated in Mn(OH)$_3$Cl. (b) MC-calculated specific heat and normalized ferromagnetic order parameter M as a function of temperature. The peak of the specific heat indicates the magnetic transition. (c) The pDOS structure of Mn(OH)$_3$Cl. (d) The spin-up and spin-down energy gaps as functions of various U_{eff} for Mn(OH)$_3$Cl.

indicated in Fig. S5 of the SM [35]. According to our DFT calculation, the configuration β owns the lower energy. The AIMD simulation at 200 K further confirms its thermal stability after the structural reconstruction (see Fig. S6 in the SM) [35]. In addition, we have also estimated the available equilibrium chemical potential region to be H-rich/Mn-poor for stable growth of Mn(OH)$_3$Cl in Fig. S7 (see the SM for details) [35].

To determine Mn(OH)$_3$Cl's magnetic ground state, four of the most probable magnetic orders are compared, as shown in Fig. S8 of the SM [35]. According to our calculation, the energy of the FM is the lowest one, implying a FM ground state (see Table II).

Our calculation shows a total magnetization of $\sim 3\mu_B$/Mn, as expected for its $3d^3$ configuration, implying Mn^{4+}. Based on the optimized structure of FM ground state, the nearest- and next-nearest-neighbor exchange coupling parameters J_1 and J_2 are derived by mapping the DFT energy to the Heisenberg model,

$$H = \sum_{<ij>} J_{ij}\vec{S}_i \cdot \vec{S}_j + \sum_i \left[A_x \left(\vec{S}_i^x \right)^2 + A_z \left(\vec{S}_i^z \right)^2 \right], \quad (10)$$

where the first item is the effective exchange interaction. Since the third-neighbor exchange parameters are small, only J_1 and J_2 are considered, as indicated in Fig. 4(a). $\vec{S}_i$ is the normalized spin vector at site i; the last item is the magnetic anisotropy, and a positive A_x (A_y) implies the magnetic hard axis.

The coefficients J_1 and J_2 are estimated as -6.68 and -1.15 meV/f.u. (see calculation details in the SM [35]). And

A_x (A_y) is 0.015 (0.113) meV/f.u.. According to the above DFT-derived coefficients, the specific heat and ferromagnetic order parameter M are calculated using the MC method, indicating a Curie temperature T_C of 72 K, as shown in Fig. 4(b).

In addition, the pDOS suggests a half-metallic state, as depicted in Fig. 4(c). The spin-down channel shows a large energy gap of ~ 2 eV, while the spin-up channel exhibits metallic state, which are mainly contributed by the partially empty Mn d and O p orbitals. Such a transport behavior makes it a promising candidate for spintronic applications.

In general, the electronic correlation may influence the electronic structures. Therefore, various values of effective Coulombic potential ($U_{eff} = 2.0, 2.5, 3.0, 3.5, 4$ eV) for Mn atoms have been applied to observe the evolution of the energy gap [see Fig. 4(d)]. As the value of U_{eff} increases, the energy gap of the spin-down channel also expands, while the spin-up channel exhibits almost zero band gap across the entire energy range. This result suggests its robust half-metallic state. In addition, the evolution of spin-polarized band structures for Mn(OH)$_3$Cl as a function of U_{eff} has also been depicted in Fig. S9 of the SM [35]. Here, the symmetry of Mn(OH)$_3$Cl is reduced to a monoclinic structure with a polar space group Pm. Therefore, the polarization along the b axis and c axis is nonzero, which originates from the intrinsic differences in the chemical environments around Cl and O atoms. The coexistence of polarity and ferromagnetic half-metallicity may offer significant multifunctional applications in the future.

IV. CONCLUSION

In summary, based on first-principles calculations, we demonstrate that noncollinear ferrielectricity, large negative piezoelectricity, and ultraviolet-light absorption can be generated in an MnO$_3$Cl crystal. In addition, we show that the intercalation of hydrogen atoms into the MnO$_3$Cl results in significant structural reconstruction. Meanwhile, a phase transition from nonmagnetic ferrielectricity to ferromagnetic polar half-metallicity also spontaneously occurs accompanying this reconstruction. These results indicate that our work opens a promising avenue for future studies of noncollinear ferrielectric properties and the potential design of multifunctional materials.

[1] H. Schmid, Multiferroic magnetoelectrics, Ferroelectrics **162**, 317 (1994).

[2] N. A. Spaldin and R. Ramesh, Advances in magnetoelectric multiferroics, Nat. Mater. **18**, 203 (2019).

[3] D. Khomskii, Classifying multiferroics: Mechanisms and effects, Physics **2**, 20 (2009).

[4] J. F. SCOTT, Applications of modern ferroelectrics, Science **315**, 954 (2007).

[5] C. H. Ahn, A. Bhattacharya, M. Di Ventra, J. N. Eckstein, C. D. Frisbie, M. E. Gershenson, A. M. Goldman, I. H. Inoue, J. Mannhart, A. J. Millis *et al.*, Electrostatic modification of novel materials, Rev. Mod. Phys. **78**, 1185 (2006).

[6] M. An and S. Dong, Ferroic orders in two-dimensional transition/rare-earth metal halides, APL Mater. **8**, 110704 (2020).

[7] A. P. Ramirez, Strong geometrically frustrated magnets, Annu. Rev. Mater. Sci. **24**, 453 (1994).

[8] S.-W. Cheong and M. Mostovoy, Multiferroics: A magnetic twist for ferroelectricity, Nat. Mater. **6**, 13 (2007).

[9] T. Kimura, Spiral magnets as magnetoelectrics, Annu. Rev. Mater. Res. **37**, 387 (2007).

[10] N. Nagaosa and Y. Tokura, Topological properties and dynamics of magnetic skyrmions, Nat. Nanotechnol. **8**, 899 (2013).

[11] N. Nagaosa, J. Sinova, S. Onoda, A. H. MacDonald, and N. P. Ong, Anomalous Hall effect, Rev. Mod. Phys. **82**, 1539 (2010).

[12] W. Feng, G.-Y. Guo, J. Zhou, Y. Yao, and Q. Niu, Large magneto-optical Kerr effect in noncollinear antiferromagnets $Mn_3X(X = Rh, Ir, Pt)$, Phys. Rev. B **92**, 144426 (2015).

[13] A. K. Yadav, C. T. Nelson, S. L. Hsu, Z. Hong, J. D. Clarkson, C. M. Schlepütz, A. R. Damodaran, P. Shafer, E. Arenholz, L. R. Dedon *et al.*, Observation of polar vortices in oxide superlattices, Nature (London) **530**, 198 (2016).

[14] D. D. Khalyavin, R. D. Johnson, F. Orlandi, P. G. Radaelli, P. Manuel, and A. A. Belik, Emergent helical texture of electric dipoles, Science **369**, 680 (2020).

[15] Y. Yang, W. Ren, M. Stengel, X. H. Yan, and L. Bellaiche, Revisiting properties of ferroelectric and multiferroic thin films under tensile strain from first principles, Phys. Rev. Lett. **109**, 057602 (2012).

[16] Y. Yang, J. Íñiguez, A.-J. Mao, and L. Bellaiche, Prediction of a novel magnetoelectric switching mechanism in multiferroics, Phys. Rev. Lett. **112**, 057202 (2014).

[17] S. Prosandeev, I. A. Kornev, and L. Bellaiche, Phase transitions in epitaxial (−110) $BiFeO_3$ films from first principles, Phys. Rev. Lett. **107**, 117602 (2011).

[18] L.-F. Lin, Y. Zhang, A. Moreo, E. Dagotto, and S. Dong, Frustrated dipole order induces noncollinear proper ferrielectricity in two dimensions, Phys. Rev. Lett. **123**, 067601 (2019).

[19] Y.-M. You, W.-Q. Liao, D. Zhao, H.-Y. Ye, Y. Zhang, Q. Zhou, X. Niu, J. Wang, P.-F. Li, D.-W. Fu *et al.*, An organic-inorganic perovskite ferroelectric with large piezoelectric response, Science **357**, 306 (2017).

[20] H.-Y. Liu, H.-Y. Zhang, X.-G. Chen, and R.-G. Xiong, Molecular design principles for ferroelectrics: Ferroelectrochemistry, J. Am. Chem. Soc. **142**, 15205 (2020).

[21] Q. Pan, Z.-X. Gu, R.-J. Zhou, Z.-J. Feng, Y.-A. Xiong, T.-T. Sha, Y.-M. You, and R.-G. Xiong, The past 10 years of molecular ferroelectrics: Structures, design, and properties, Chem. Soc. Rev. **53**, 5781 (2024).

[22] K. Liu, L. Liu, and T. Zhai, Emerging two-dimensional inorganic molecular crystals: The concept and beyond, J. Phys. Chem. Lett. **13**, 2173 (2022).

[23] W. Han, P. Huang, L. Li, F. Wang, P. Luo, K. Liu, X. Zhou, H. Li, X. Zhang, Y. Cui, and T. Zhai, Two-dimensional inorganic molecular crystals, Nat. Commun. **10**, 4728 (2019).

[24] J. Spandl, J. Supeł, T. Drews, and K. Seppelt, MnO_3 Cl, isolation and crystal structure, Z. Anorg. Allg. Chem. **632**, 2222 (2006).

[25] G. Kresse and J. Furthmüller, Efficient iterative schemes for *ab initio* total-energy calculations using a plane-wave basis set, Phys. Rev. B **54**, 11169 (1996).

[26] J. P. Perdew, K. Burke, and M. Ernzerhof, Generalized gradient approximation made simple, Phys. Rev. Lett. **77**, 3865 (1996).

[27] S. Grimme, J. Antony, S. Ehrlich, and H. Krieg, A consistent and accurate *ab initio* parametrization of density functional dispersion correction (DFT-D) for the 94 elements H-Pu, J. Chem. Phys. **132**, 154104 (2010).

[28] R. D. King-Smith and D. Vanderbilt, Theory of polarization of crystalline solids, Phys. Rev. B **47**, 1651 (1993).

[29] A. Gulans, S. Kontur, C. Meisenbichler, D. Nabok, P. Pavone, S. Rigamonti, S. Sagmeister, U. Werner, and C. Draxl, EXCITING: A full-potential all-electron package implementing density-functional theory and many-body perturbation theory, J. Phys.: Condens. Matter **26**, 363202 (2014).

[30] C. Sujith, S. Joseph, A. Sneha, T. Mathew, and V. Mathew, Large birefringence in the quasi-one-dimensional material Sb_2Se_3: A DFT investigation of electronic and optical anisotropy, J. Phys. Chem. Solids **174**, 111161 (2023).

[31] X. Huang, T. R. Paudel, S. Dong, and E. Y. Tsymbal, Hexagonal rare-earth manganites as promising photovoltaics and light polarizers, Phys. Rev. B **92**, 125201 (2015).

[32] S. L. Dudarev, G. A. Botton, S. Y. Savrasov, C. J. Humphreys, and A. P. Sutton, Electron-energy-loss spectra and the structural stability of nickel oxide: An LSDA + U study, Phys. Rev. B **57**, 1505 (1998).

[33] Z. Wang, Y. Chai, and S. Dong, First-principles demonstration of Raman-surface topological multiferroicity, Phys. Rev. B **108**, L060407 (2023).

[34] G. J. Martyna, M. L. Klein, and M. Tuckerman, Nosé-Hoover chains: The canonical ensemble via continuous dynamics, J. Chem. Phys. **97**, 2635 (1992).

[35] See the Supplemental Material at http://link.aps.org/supplemental/10.1103/PhysRevB.110.134113 for the SHG tensors of MnO_3Cl and KH_2PO_4; elastic stiffness tensor elements; dielectric spectra; different configurations of $Mn(OH)_3Cl$; result of AIMD simulation; available equilibrium chemical potential region; schematic of four most probable magnetic orders of $Mn(OH)_3Cl$; and band structures for various values of U_{eff}. References [54–57] are cited therein.

[36] V. Maisonneuve, V. B. Cajipe, A. Simon, R. Von Der Muhll, and J. Ravez, Ferrielectric ordering in lamellar $CuInP_2S_6$, Phys. Rev. B **56**, 10860 (1997).

[37] G. Henkelman, B. P. Uberuaga, and H. Jónsson, A climbing image nudged elastic band method for finding saddle points and minimum energy paths, J. Chem. Phys. **113**, 9901 (2000).

[38] S. Bergfeld and W. Daum, Second-harmonic generation in GaAs: Experiment versus theoretical predictions of $\chi^{(2)}_{xyz}$, Phys. Rev. Lett. **90**, 036801 (2003).

[39] I. Abdelwahab, B. Tilmann, Y. Wu, D. Giovanni, I. Verzhbitskiy, M. Zhu, R. Berté, F. Xuan, L. de S. Menezes, G. Eda *et al.*, Giant second-harmonic generation in ferroelectric $NbOI_2$, Nat. Photon. **16**, 644 (2022).

[40] R. L. Sutherland, *Handbook of Nonlinear Optics* (CRC Press, Boca Raton, FL, 2003).

[41] X. Yang and S. Dong, Oxidation tuning of ferroic transitions in Gd_2C monolayer, J. Chem. Phys. **160**, 014705 (2024).

[42] R. C. Eckardt, H. Masuda, Y. X. Fan, and R. L. Byer, Absolute and relative nonlinear optical coefficients of KDP, KD*P, BaB_2O_4, $LiIO_3$, $MgO : LiNbO_3$, and KTP measured by phase-matched second-harmonic generation, IEEE J. Quantum Electron. **26**, 922 (1990).

[43] I. Katsouras, K. Asadi, M. Li, T. B. van Driel, K. S. Kjær, D. Zhao, T. Lenz, Y. Gu, P. W. M. Blom, D. Damjanovic *et al.*, The negative piezoelectric effect of the ferroelectric polymer poly(vinylidene fluoride), Nat. Mater. **15**, 78 (2016).

[44] L. You, Y. Zhang, S. Zhou, A. Chaturvedi, S. A. Morris, F. Liu, L. Chang, D. Ichinose, H. Funakubo, W. Hu *et al.*, Origin of giant negative piezoelectricity in a layered van der Waals ferroelectric, Sci. Adv. **5**, eaav3780 (2019).

[45] X. Gonze and C. Lee, Dynamical matrices, Born effective charges, dielectric permittivity tensors, and interatomic force constants from density-functional perturbation theory, Phys. Rev. B **55**, 10355 (1997).

[46] M. de Jong, W. Chen, H. Geerlings, M. Asta, and K. A. Persson, A database to enable discovery and design of piezoelectric materials, Sci. Data **2**, 150053 (2015).

[47] V. Wang, N. Xu, J.-C. Liu, G. Tang, and W.-T. Geng, VASPKIT: A user-friendly interface facilitating high-throughput computing and analysis using VASP code, Comput. Phys. Commun. **267**, 108033 (2021).

[48] N. Ding, J. Chen, C. Gui, H. You, X. Yao, and S. Dong, Phase competition and negative piezoelectricity in interlayer-sliding ferroelectric ZrI_2, Phys. Rev. Mater. **5**, 084405 (2021).

[49] D. Puggioni, A. Stroppa, and J. M. Rondinelli, Design of a polar half-metallic ferromagnet with accessible and enhanced electric polarization, Phys. Rev. Mater. **2**, 114403 (2018).

[50] J. Zhang, S. Shen, D. Puggioni, M. Wang, H. Sha, X. Xu, Y. Lyu, H. Peng, W. Xing, L. N. Walters *et al.*, A correlated ferromagnetic polar metal by design, Nat. Mater. **23**, 912 (2024).

[51] B.-C. Gong, H.-C. Yang, J.-F. Zhang, K. Liu, and Z.-Y. Lu, Inducing high-T_c ferromagnetism in the van der Waals crystal $Mn(ReO_4)_2$ via charge doping: A first-principles study, Phys. Rev. B **104**, 075133 (2021).

[52] H.-P. You, J. Chen, J.-J. Zhang, N. Ding, X.-W. Zhang, X.-Y. Yao, and S. Dong, Structural reconstruction and anisotropic conductance in $4f$-ferromagnetic monolayer, Mater. Today Phys. **24**, 100693 (2022).

[53] L. Zhang, C. Tang, S. Sanvito, Y. Gu, and A. Du, Hydrogen-intercalated 2D magnetic bilayer: Controlled magnetic phase transition and half-metallicity via ferroelectric switching, ACS Appl. Mater. Interfaces **14**, 1800 (2022).

[54] R. P. Liferovich and R. H. Mitchell, A structural study of ternary lanthanide orthoscandate perovskites, J. Solid State Chem. **177**, 2188 (2004).

[55] M. Atoji and W. N. Lipscomb, The molecular structure of B_4Cl_4, J. Chem. Phys. **21**, 172 (1953).

[56] S.-H. Wei, Overcoming the doping bottleneck in semiconductors, Comput. Mater. Sci. **30**, 337 (2004).

[57] X. Huang, T. R. Paudel, P. A. Dowben, S. Dong, and E. Y. Tsymbal, Electronic structure and stability of the $CH_3NH_3PbBr_3$ (001) surface, Phys. Rev. B **94**, 195309 (2016).